The Astrophysical Journal, 774:118 (8pp), 2013 September 10 doi:10.1088/0004-637X/774/2/118
© 2013. The American Astronomical Society. All rights reserved. Printed in the U.S.A.

EXAMINING THE BROADBAND EMISSION SPECTRUM OF WASP-19b: A NEW z-BAND ECLIPSE DETECTION

George Zhou[1], Lucyna Kedziora-Chudczer[2], Daniel D. R. Bayliss[1], and Jeremy Bailey[2]
[1] Research School of Astronomy and Astrophysics, Australian National University, Cotter Rd, Weston Creek, ACT 2611, Australia; george@mso.anu.edu.au
[2] School of Physics, University of New South Wales, Sydney, NSW 2052, Australia
Received 2013 May 16; accepted 2013 July 16; published 2013 August 22

ABSTRACT

WASP-19b is one of the most irradiated hot-Jupiters known. Its secondary eclipse is the deepest of all transiting planets and has been measured in multiple optical and infrared bands. We obtained a z-band eclipse observation with a measured depth of $0.080\% \pm 0.029\%$, using the 2 m Faulkes Telescope South, which is consistent with the results of previous observations. We combined our measurement of the z-band eclipse with previous observations to explore atmosphere models of WASP-19b that are consistent with its broadband spectrum. We use the VSTAR radiative transfer code to examine the effect of varying pressure–temperature profiles and C/O abundance ratios on the emission spectrum of the planet. We find that models with super-solar carbon enrichment best match the observations, which is consistent with previous model retrieval studies. We also include upper atmosphere haze as another dimension in the interpretation of exoplanet emission spectra and find that particles $<0.5\,\mu$m in size are unlikely to be present in WASP-19b.

Key words: planets and satellites: atmospheres – planets and satellites: individual (WASP-19b)

Online-only material: color figures

1. INTRODUCTION

Recent observations of transiting planet systems have led to the first in-depth characterization of exoplanet atmospheres. Observations of the secondary eclipse event, when the planet is blocked by the host star, are the predominant method of measuring the emergent flux of close-in exoplanets. In particular, secondary eclipses observed at multiple wavelength bands have provided the first spectral energy distribution of exoplanets (Charbonneau et al. 2005, 2008). Similar observations have revealed the presence of molecular absorption features (e.g., Grillmair et al. 2008; Swain et al. 2009) in the emission spectra of hot-Jupiters, and hinted at the diversity of chemical compositions across exoplanet atmospheres (e.g., Barman 2008; Madhusudhan & Seager 2009).

WASP-19b (Hebb et al. 2010) is a $1.17\,M_{\rm Jup}$, $1.39\,R_{\rm Jup}$ exoplanet in a 0.79 day prograde orbit (Hellier et al. 2011) which transits a $V_{\rm mag} = 12.3$ G dwarf. The equilibrium temperature for the planet is at least 2000 K, making it one of the hottest hot-Jupiters known, and the most favorable target for eclipse observations. The proximity of WASP-19b to the host star also makes it an interesting case study of irradiated atmospheres. In particular, eclipse observations have shown that WASP-19b is inconsistent with the hypothesis that highly irradiated planets exhibit thermal inversion features (Hubeny et al. 2003; Burrows et al. 2007; Fortney et al. 2008), although some exceptions are known (e.g., HD 189733b, TrES-3b, and XO-1b; Charbonneau et al. 2008; Fressin et al. 2010; Machalek et al. 2008). Madhusudhan (2012) proposed WASP-19b as a planet hosting a carbon-rich atmosphere that is depleted in TiO, which is a primary absorber for inversion layers. In addition, the carbon-to-oxygen ratio (C/O) is a potential indicator for the location in the proto-planetary disk where these hot-Jupiters originated (e.g., Lodders 2004; Öberg et al. 2011).

The C/O enrichment hypothesis is based upon existing multi-band eclipse observations of WASP-19b, including the ASTEP400 broadband centered at $0.67\,\mu$m (Abe et al. 2013), z band (Burton et al. 2012; Lendl et al. 2013), $1.190\,\mu$m narrow band (Lendl et al. 2013), H band (Anderson et al. 2010), K band (Gibson et al. 2010), *Spitzer* 3.6, 4.5, 5.8, and $8.0\,\mu$m bands (Anderson et al. 2013), as well as spectrophotometric observations at 1.25–2.35 μm by Bean et al. (2013). However, it is difficult to produce a single model that can fit all the measurements within their uncertainty constraints. Ground-based observations at the 0.1% level remain difficult, and are affected by a range of systematic effects, such as atmospheric variations, unstable telescope tracking, and detector defects. Independent confirmation observations are required to strengthen the reliability of individual measurements.

The depth of the z-band eclipse is particularly important in determining the C/O ratio of WASP-19b, a deeper eclipse is indicative of an atmosphere deficient in TiO absorption and enriched in C/O abundance. New Technology Telescope ULTRACAM observations by Burton et al. (2012) reported an eclipse depth of $0.088\% \pm 0.019\%$, while a combined set of observations with EulerCam and TRAPPIST over 10 epochs by Lendl et al. (2013) reported a shallower eclipse depth of $0.035\% \pm 0.012\%$. While these observations are consistent at the $\sim 2\sigma$ regime, the difference between the two measurements makes it difficult to constrain the atmosphere models of WASP-19b.

In this study, we present an independent observation of a WASP-19b eclipse event using Faulkes Telescope South (FTS) aimed at confirming its z-band secondary eclipse depth. We present a careful treatment of the photometry to achieve near photon-limited light curves. To investigate the previous claim of a carbon-rich atmosphere, we use the VSTAR radiative transfer code (Bailey & Kedziora-Chudczer 2012) and the ensemble of observations to model the atmosphere of WASP-19b and examine the effects of temperature–pressure profiles and C/O abundance on its emergent spectrum. One drawback of the existing model retrieval studies (Madhusudhan & Seager 2009) are their lack of treatment for non-isotropic scattering. The lack of absorption features in the transmission spectrum

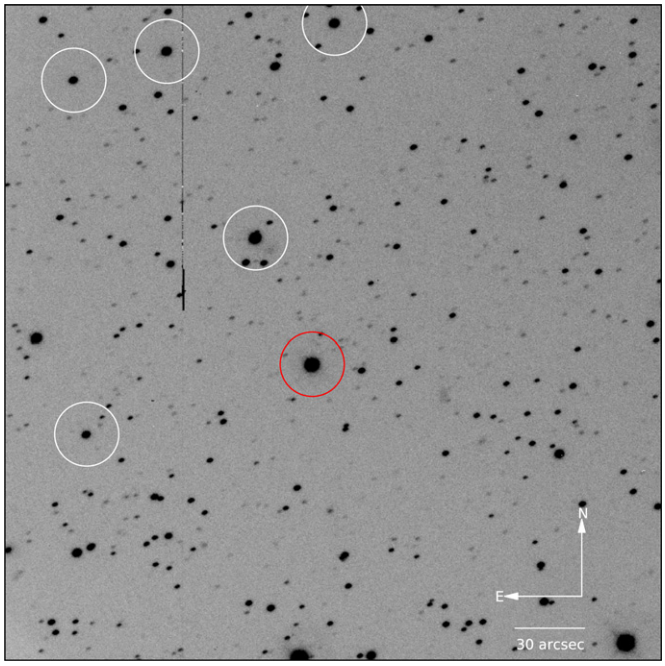

Figure 1. FTS z-band image of the WASP-19 field. The target, located in the center of the field, is circled in red; the chosen set of reference stars is circled in white. The size of the circle indicates the size of the background aperture. The column of dead pixels in the top left of the image was masked out for the photometry.

(A color version of this figure is available in the online journal.)

in HD 189733b (Pont et al. 2008), as well as the weaker-than-expected detections of sodium in various hot-Jupiters (e.g., Charbonneau et al. 2002; Fortney et al. 2003; Zhou & Bayliss 2012), all point to the importance of clouds and haze in modeling planetary atmospheres. We also exploit the rigorous treatment of Rayleigh scattering by VSTAR to investigate the effect of upper atmosphere haze on the emission spectrum of WASP-19b.

2. DETECTION OF z-BAND ECLIPSE

2.1. Observations

We monitored an eclipse of WASP-19b using the 2 m FTS, located at Siding Spring Observatory, Australia, on 2012 December 29, from 12:03 to 15:50 UT, with the expected eclipse occurring during 13:25–15:02 UT. Observations were performed in the Pan-STARRS z-band, centered at 0.866 μm (Tonry et al. 2012), using the Merope 2 K × 2 K camera, with a 4.′7 × 4.′7 field of view, an unbinned pixel size of 0.″139 pixel^{-1}, and read out with 2×2 bins. 161×60 s exposures were taken. The seeing on the night previous to the observing sequence was ∼1″. The telescope was slightly defocused to avoid saturation and to reduce the effect of intra- and residual inter-pixel variations, resulting in point-spread functions (PSFs) with a FWHM of ∼2″. Bias subtraction and flat-field corrections were performed using the CCDPROC package in IRAF[3] with the most recent archival calibration frames. An example image is shown in Figure 1.

[3] IRAF is distributed by the National Optical Astronomy Observatory, which is operated by the Association of Universities for Research in Astronomy, Inc., under cooperative agreement with the National Science Foundation.

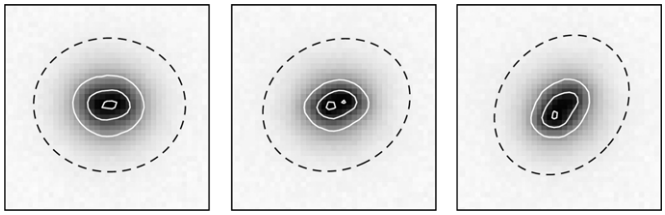

Figure 2. PSF variations of the target star over the course of the observations, shown at the start (left), middle (center), and end of the night (right). The solid white lines mark the 0.95, 0.50, and 0.10 peak height contours. The dashed black line marks the photometry aperture used. The crops are 20 pixels in size.

2.2. Analysis

2.2.1. PSF Variations and Adaptive Aperture Photometry

Upon close examination of the images, we find that the stellar PSF is asymmetric across the image. The distortion and elongation of the PSF is a result of the defocusing applied. In addition, the position angle of the elongated PSF changes with the rotation of the telescope (Figure 2), as FTS is on an alt-az mount. To further investigate the PSF variations, we create a template PSF from a single exposure taken mid-run, and fit it to the remaining exposures, allowing for rotation and spatial dilation. We find no significant deviations in the fit residuals, with the exception of the initial images taken at high airmass, suggesting that the general shape of the PSF remained constant throughout the night.

We performed elliptical aperture photometry on the reduced images. Compared to conventional circular apertures, variable elliptical apertures best account for all of the stellar flux while minimizing background noise. The ellipse parameters, semimajor axis A, semiminor axis B, and position angle θ were measured using Source Extractor (Bertin & Arnouts 1996), and are plotted in Figure 3 along with other relevant global parameters. A and B are the maximum and minimum root mean square (rms) of the spatial profile. The size of the aperture, R, is a scaling factor that maintains the shape and orientation of the ellipse, and is related to the ellipse parameters CXX, CYY, and CXY by

$$\begin{aligned} R^2 &= CXX(x-\bar{x})^2 + CYY(y-\bar{y})^2 \\ &\quad + CXY(x-\bar{x})(y-\bar{y}) \\ CXX &= \frac{\cos^2\theta}{A^2} + \frac{\sin^2\theta}{B^2} \\ CYY &= \frac{\sin^2\theta}{A^2} + \frac{\cos^2\theta}{B^2} \\ CXY &= 2\cos\theta\sin\theta\left(\frac{1}{A^2} - \frac{1}{B^2}\right). \end{aligned} \quad (1)$$

The lowest out-of-eclipse scatter was achieved using aperture sizes of $R = 4.2$, enclosing ∼99% of the flux. The adopted elliptical aperture parameters A, B, and θ were determined from linear fits in time to the averaged measurements from Sourced Extractor. Higher order fits to the ellipse parameters were tested, and did not result in significantly different light curves or eclipse depths. Exposures with HJD $<$ 2456291.03 were discarded from the analysis, since they were taken at high airmass, when the PSF shape varied rapidly.

The background was estimated using a 100 pixel diameter outer aperture on a background image with all detected sources masked out. Since WASP-19 resides in a relatively crowded field, masking out field stars is essential to achieving optimal

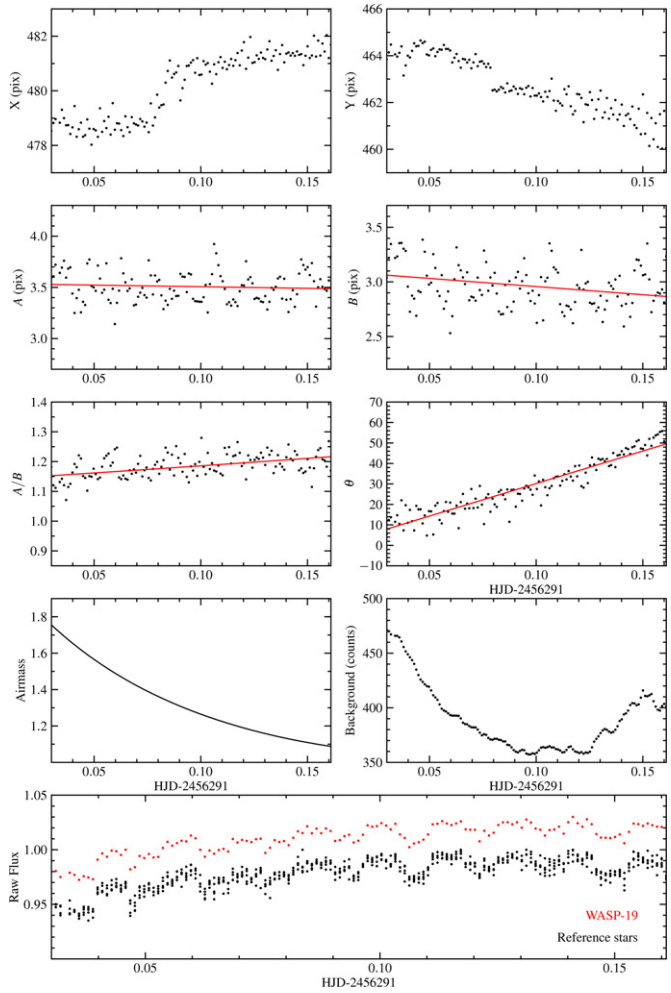

Figure 3. Variations in the target X position, Y position, PSF semimajor and minor axes (A, B), ellipticity (A/B), ellipse position angle (θ), airmass, background counts, normalized raw target (red) and ensemble reference (black, arbitrarily offset by 0.05) fluxes are plotted. Linear fits to the ellipse parameters, used to define the elliptical photometry apertures, are plotted in red.

(A color version of this figure is available in the online journal.)

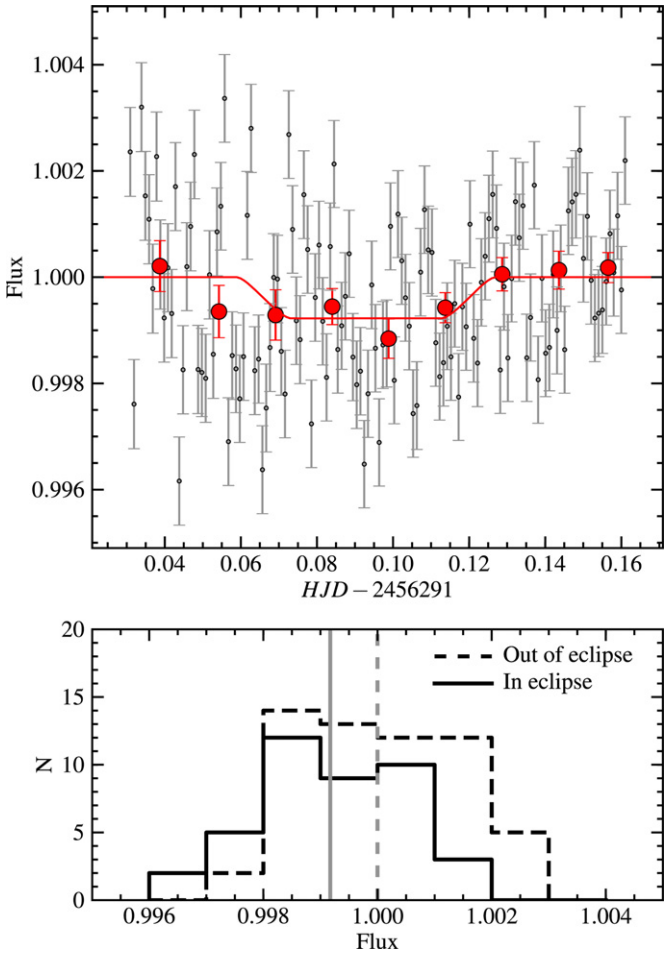

Figure 4. Top: eclipse light curve of WASP-19b, with the best-fitting model plotted in red. Data binned at 0.015 days are plotted as large red points for clarity. Bottom: histogram showing the distribution of flux measurements in- (solid) and out-of-eclipse (dashed), with the centroids of the distributions marked by the corresponding vertical lines.

(A color version of this figure is available in the online journal.)

background subtraction. We note that Burton et al. (2012) followed a similar technique in their analysis. The background count around WASP-19 is plotted in Figure 3.

Differential photometry was performed using five reference stars (labeled in Figure 1), chosen for their lack of nearby neighbors, similar color indices to the target, and the eventual stability of the light curves. A master reference light curve (M) was created by averaging the ensemble of reference stars (R_i), each with errors ΔR_i:

$$M = \sum_i \frac{c_i}{\Delta R_i} R_i \,, \tag{2}$$

where weights c_i were chosen to minimize the rms scatter of the corrected object light curve. The use of weights to minimize the object light curve scatter is similar to applying the Trend Filtering Algorithm to the out-of-transit data set (Kovács et al. 2005). To remove uncorrelated trends in the individual reference star light curves, we divided each reference star by a master reference light curve made of all other reference stars. Any slow varying residual trends in that reference star were then corrected for by a linear fit. In addition, individual outlier points significantly different from other reference stars were removed by sigma clipping. Finally, a linear trend was removed from the target light curve by fitting for the out-of-eclipse points. We note that the target light curve was treated by the same processes as the reference light curves. The ensemble of raw reference light curves, as well as the raw target light curve, is plotted in Figure 3.

2.2.2. Eclipse Model Fitting

We fit a Mandel & Agol (2002) eclipse model to the FTS light curve via a downhill simplex minimization of the χ^2 of the fit, followed by a Markov chain Monte Carlo (MCMC) ensemble sampler (*emcee* implementation; Foreman-Mackey et al. 2013) to determine the uncertainties. For the MCMC routine, we artificially inflate the photometric uncertainties such that the reduced $\chi^2 = 1$. This accounts for the contribution of other systematic effects in addition to the photon-noise uncertainty. The free parameters of the fit are the transit center t_0, depth D, normalized planet orbital radius $a/R_\star$, and the impact parameter b. The parameters t_0, $a/R_\star$, and b are constrained by Gaussian priors based on the joint analysis performed by Anderson et al. (2013). The system period and planet-star radius ratio are fixed to the Anderson et al. (2013) values. The fitted light curve is shown in Figure 4.

Table 1
Reduced χ^2 and Eclipse Depth After Decorrelation

External Parameter	Reduced χ^2	D %
None	3.28	0.080
X, Y	3.25	0.087
A	3.30	0.078
A/B	3.29	0.078
θ	3.28	0.074
Airmass	3.31	0.080
Background	3.30	0.071

The final eclipse depth is $0.080\% \pm 0.029\%$. The corresponding z-band brightness temperature is 2680^{+140}_{-180} K. A MARCS model atmosphere spectrum (Gustafsson et al. 2008) was adopted for the host star in the brightness temperature calculation for the planet. The derived brightness temperature agrees well with the ASTEP 1.6 and 2.09 μm temperatures (Abe et al. 2013; Anderson et al. 2013).

The depth can also be derived separately by binning the in- and out-of-eclipse points. In Figure 4, we bin the points according to the predicted ephemeris. The eclipse depth, given by the difference in the sigma clipped mean of the two bins, is $0.083\% \pm 0.026\%$, with the uncertainty taken as the error in the mean of the two bins, added in quadrature. This agrees with the transit depth measured by the model fit.

2.2.3. Correlation to External Parameters

Most high-precision transit and eclipse photometry to date have been processed with some form of external parameter decorrelation to remove residual systematic trends. This is often done by multiplying the light curve with a linear combination of external parameters, such as airmass, position, and FWHM (e.g., López-Morales et al. 2010; Burton et al. 2012); occasionally, higher order terms have also been employed (e.g., up to fourth order; Lendl et al. 2013).

We test for the effectiveness of detrending by simultaneously fitting for the eclipse and a combination of external terms involving the X position, Y position, semimajor axis A, ellipticity A/B, airmass, and background counts, while holding t_0 constant. In each case, the removal of a linear trend is also allowed. Analysis is performed over the entire light curve, since the out-of-eclipse points constitute less than half of the observations and cannot sufficiently represent the entire data set. Table 1 shows the reduced χ^2 after each minimization routine. No significant improvements to the χ^2 were achieved from any decorrelations. The transit depth also remained roughly independent of these external parameters.

We can also check for time-correlated noise in the residuals using the β factor diagnostic (Winn et al. 2008). For residuals binned into M bins with N points per bin, the scatter σ_N as a function of the noise of the unbinned data σ_1 is

$$\sigma_N = \beta \frac{\sigma_1}{\sqrt{N}} \sqrt{\frac{M}{M-1}}. \quad (3)$$

For uncorrelated data, $\beta = 1$. Our residuals have an average of $\beta = 1.15$, suggesting minimal time-correlated trends in the residuals. Figure 5 shows the rms of the residuals as a function of bin widths. The lack of a need for any decorrelation can be primarily attributed to the use of variable, elliptical apertures.

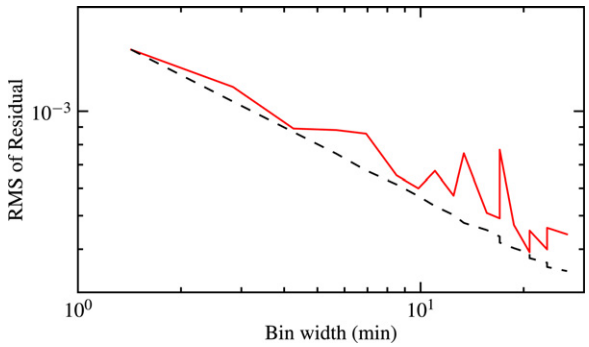

Figure 5. rms of the residuals as a function of bin width are plotted in red. The dashed line shows the $1/\sqrt{N}$ drop off expected for an uncorrelated signal. (A color version of this figure is available in the online journal.)

3. VSTAR ATMOSPHERE MODEL

We use the VSTAR line-by-line radiative transfer code (Bailey & Kedziora-Chudczer 2012) to derive a model atmosphere of WASP-19b that fits our measurement and the data published previously. VSTAR is a comprehensive atmospheric radiative transfer model incorporating a chemical equilibrium model, an extensive database of molecular spectral lines, and a full treatment of multiple-scattering radiative transfer using the discrete ordinate method. It has been extensively tested and applied to objects ranging from solar system planets (Chamberlain et al. 2013; Cotton et al. 2012; Kedziora-Chudczer & Bailey 2011) to M-dwarfs (Bailey & Kedziora-Chudczer 2012). It is impossible to obtain a unique model that can best fit the currently available broadband data that only sparsely covers the optical and infrared spectrum. Instead, we focus on a discussion of the effects observed in a spectrum by changing specific conditions in the planetary atmosphere.

Highly irradiated planets, like WASP-19b, have been hypothesized to show thermal inversion in their atmospheric profiles due to condensation of VO and TiO within a cold trap (Fortney et al. 2008). However, the *Spitzer* IRAC data (Anderson et al. 2013) and near-infrared (NIR) ground measurements at 1.6 and 2.1 μm (Anderson et al. 2010; Gibson et al. 2010) appear to be inconsistent with thermal inversion in the planet's atmosphere. Various explanations have been proposed for the lack of thermal inversion in some highly irradiated planets, such as the dependency on the presence of a cold trap (Showman et al. 2009; Spiegel et al. 2009), destruction of absorbers by stellar activity (Knutson et al. 2010), disequilibrium photochemistry (Zahnle et al. 2009), or the enrichment of C/O that leads to a depleted TiO abundance (Madhusudhan 2012).

In our modeling, we use four different atmospheric pressure–temperature (P–T) profiles without inversion (Figure 6(a)): (1) the red profile in Figure 12 of Madhusudhan (2012); (2) a "hotter" profile, which corresponds to conditions discussed by Anderson et al. (2013); (3) a "cooler" profile, which reflects the range of temperatures and pressures assumed by Bean et al. (2013) to explain their NIR data; and (4) a "narrow" P–T profile, with a reduced range of temperatures that overlap with the Madhusudhan (2012) model over the range of 0.05–0.5 bar.

Our models assume a plane-parallel, stratified atmosphere with 25 layers characterized by temperature, pressure, and mixing ratios of the following molecular and atomic species: H_2O, CO, CH_4, CO_2, C_2H_2, HCN, TiO, VO, Na, K, H_2, He, Rb, Cs, CaH, CrH, MgH, and FeH. The mixing ratios of these opacity sources are calculated in chemical equilibrium. The

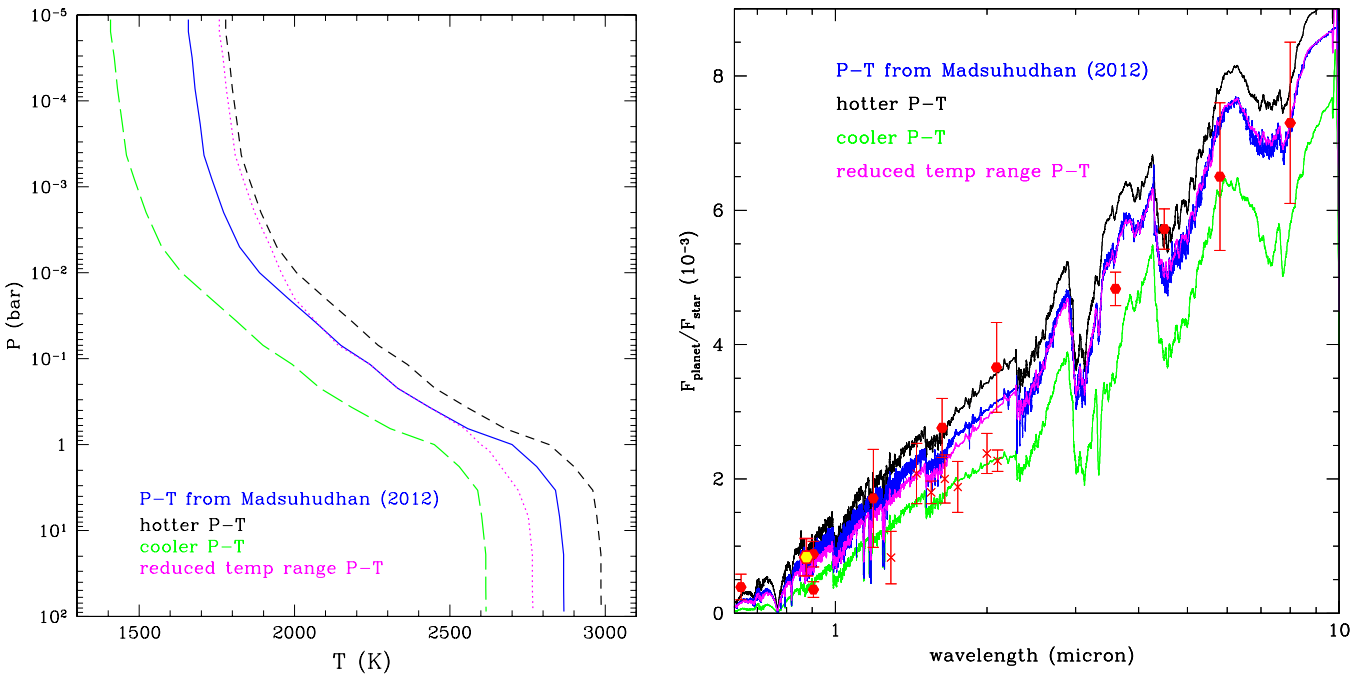

Figure 6. Left: four *P–T* atmosphere profiles described in more detail in Section 3. Right: the WASP-19b VSTAR models corresponding to the *P–T* profiles shown on the left. A C/O ratio of 1.1 was assumed in all four models, along with molecular absorption due to H_2O, CO, CH_4, CO_2, C_2H_2, HCN, TiO, VO. The yellow hexagon denotes the data point from the FTS observation reported in this paper, red crosses show data from Bean et al. (2013), while red hexagons mark results of all other observations described in Section 1.

(A color version of this figure is available in the online journal.)

Table 2
List of Molecular and Atomic Absorbers Used in the VSTAR Modeling with References to the Line Databases

Line Absorbers	Reference
CH_4	See 2.2.6 in Bailey & Kedziora-Chudczer (2012)
CO_2	Pollack et al. (1993)
H_2O	Barber et al. (2006)
CO	Goorvitch (1994)
HCN	Harris et al. (2006)
C_2H_2	Rothman et al. (2009)
CaH	Weck et al. (2003b)
MgH	Weck et al. (2003a); Skory et al. (2003)
FeH	Dulick et al. (2003); Hargreaves et al. (2010)
CrH	Burrows et al. (2002)
TiO	Plez (1998)
VO	B. Plez (2010, private communication)
K, Na, Rb, Cs	Piskunov et al. (1995); Kupka et al. (1999)

atmospheres of hot-Jupiters like WASP-19b are most likely dominated by H_2, which is a source of the H_2–H_2 and H_2–He collisionally induced absorption that we included with opacities calculated by Borysow & Borysow (1998). We also considered Rayleigh scattering by H_2, He, and H in the atmosphere of the planet, and free–free and bound–free absorption from H, H^-, and H_2^-. Our spectral line absorption database is described in detail in Bailey & Kedziora-Chudczer (2012). Table 2 lists the references to the sources of spectral lines for absorbers used in our models. A spectrum of the WASP-19, G8V-type star was obtained from the STScI stellar atmosphere models by Castelli & Kurucz (2004).

Figure 6(b) shows the model spectra for the four *P–T* profiles considered above. All of the models presented in this figure have C/O = 1.1. Thus, they can be easily compared with the red spectrum in Figure 12 of Madhusudhan (2012). The differences between our model and the Madhusudhan (2012) model with the same *P–T* profile can be attributed to use of line databases which may have varied levels of completeness. The model with the "hotter" *P–T* profile tends to fit the NIR data from Anderson et al. (2010) and Gibson et al. (2010) better, while the "cooler" *P–T* profile produces a spectrum that matches closer to the data obtained by Bean et al. (2013). However, both these profiles either overestimate or underestimate the absorption observed in the *Spitzer* data between 3.6 and 8 μm. We also found very little difference between the "narrow" *P–T* profile and the one from Madhusudhan (2012), with only slightly increased absorption between 1 and 2 μm in the "narrow" *P–T* profile.

In Figure 7, we show the effect of varying C/O ratio on spectra using an example of a model with our hottest *P–T* profile, although qualitative results are the same for other profiles considered here. The spectrum obtained for C/O = 0.5 is dominated by the oxygen bearing molecules with strong H_2O bands visible in the NIR and far-IR, and CO_2 and CO bands around 4.5 μm. Around C/O = 1, the abundances of carbon and oxygen containing molecules change dramatically by many orders of magnitudes. This explains the rapid decrease of H_2O absorptions in the spectra when the C/O ratio varies between 0.9 and 1.1 in the right panel of Figure 7, while only modest changes are visible in the left panel of Figure 7 between C/O = 1.1 and C/O = 4.0. The spectra of atmospheres with a high content of carbon are dominated by CH_4 absorption in addition to molecules such as HCN and C_2H_2 considered also in Madhusudhan (2012). While strong water absorption bands are absent, the CO features around 2.3 and 4.8 μm become more prominent. Currently available spectral measurements for WASP-19b seem to be more consistent with the atmosphere models that are derived with a C/O ratio higher than solar.

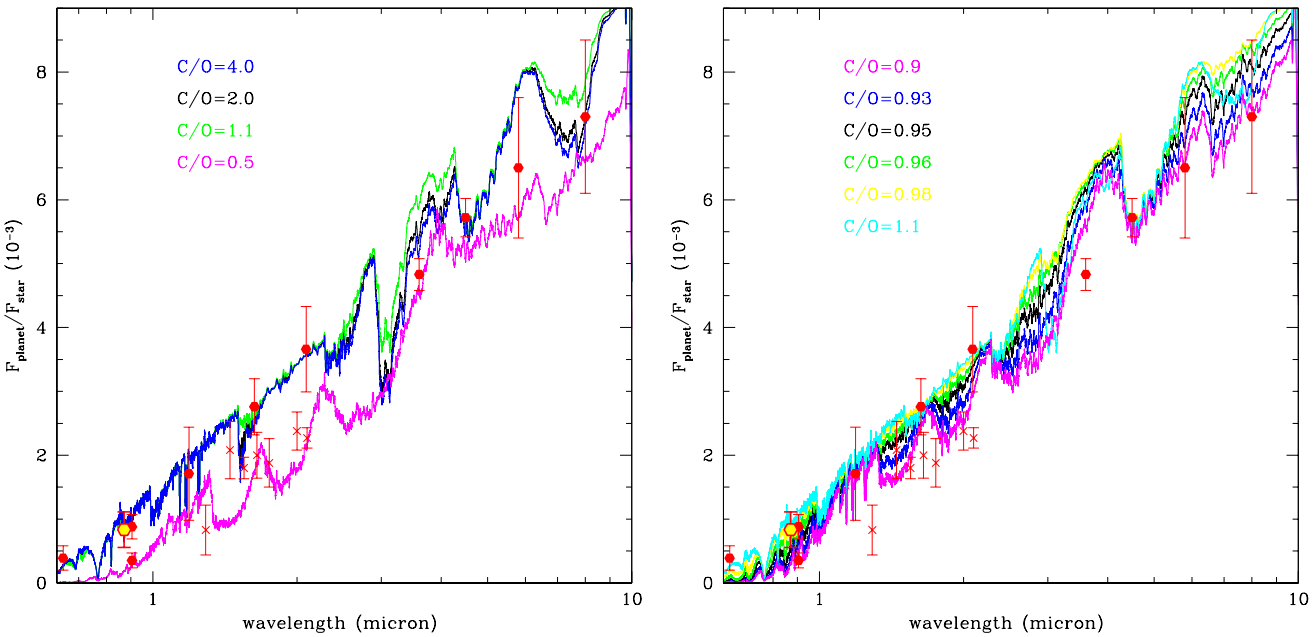

Figure 7. Example of WASP-19b atmosphere models with the "hotter" *P–T* profile and changing ratio of C/O. Left: the model with the close to solar ratio C/O = 0.5 seems to be especially inconsistent with the data from optical observations. Models with C/O ratios above 1 fit better all of the data except the NIR observations of Bean et al. (2013). Right: strong changes in the water absorption bands across the infrared range of the spectrum around the region of C/O = 1 are shown, where the abundances of oxygen and carbon bearing species vary by orders of magnitude.

(A color version of this figure is available in the online journal.)

The models presented so far in Figure 6 assumed a clear atmosphere. However, recently published data for the hot-Jupiter HD 189733b (Pont et al. 2008) indicate the presence of haze in the top layers of its atmosphere. The composition of the hazes depends on the abundance and refractory properties of different compounds (Burrows & Sharp 1999). In hot-Jupiters and brown dwarfs, suggested condensates may be formed by highly refractory species such as perovskite ($CaTiO_3$) and corundum (Al_2O_3), which condense in temperatures close to 1600 K. More abundant Si, Mg, and Fe elements combine into compounds such as enstatite ($MgSiO_3$) and forsterite (Mg_2SiO_4) that condense in lower temperatures. Even at the relatively lower temperatures at the top of the atmosphere of WASP-19b, it is not clear which species could potentially exist in a form of haze.

In Figure 8, we assume that such a haze exists and is composed of an unknown particulate with a refractive index similar to enstatite. Four examples of the model spectrum are shown for WASP-19b, where the optical depth of a cloud in the top layer of the atmosphere is varied. The particles with a mean size of 0.5 μm are assumed in the left panel. On the right, all models are derived with the varied mean size of particles, while the same optical depth $\tau = 1$ at 1.5 μm is assumed. The absorption and scattering properties as a function of wavelength are calculated using Mie theory. At wavelengths comparable to the size of cloud particles, scattering processes operate efficiently, which leads to the increase of planetary albedo in the corresponding part of its spectrum. On the other hand the added opacity in the top layers obscures thermal emission from the planet, which has the effect of lowering the received flux in the infrared part of a spectrum. Differences in particle sizes affect both the scattering and absorption properties of the haze. Particles smaller than 0.5 μm appear to generate a highly reflective haze at visible wavelengths, which may not be consistent with the measurement from Abe et al. (2013).

Observations of secondary eclipses at different wavelengths are sensitive to different properties of the planetary atmosphere. Observations of the flux in the z band can provide a sensitive probe of the C/O ratio in the atmosphere of the planet, as shown in Figure 7. In the optical spectrum, strongly absorbing bands of VO and TiO dominate the measured flux in temperatures above 1700 K when the C/O ratio is similar to solar. After VO and TiO start to condense below this temperature, absorption from alkali lines and water bands takes over. However, if C/O is higher than solar, then alkali lines will be distinct even at lower temperatures due to reduced abundance of VO and TiO. On the other hand, in the presence of stratospheric haze, Rayleigh scattering may dominate optical spectrum almost entirely as seen in Figure 8. A few more strategically placed photometric data points in optical and NIR spectrum will help to discriminate between these broad conditions of the WASP-19b atmosphere. However, more detailed and unique models can only be derived when the amount of photometric data becomes sufficient to break degeneracies in the interpretation of current spectral features. This is currently a rather remote prospect as discussed in Line et al. (2013).

4. DISCUSSIONS

We presented an examination of the emission spectrum of WASP-19b measured in eclipse. Using FTS observations, we measured the z-band eclipse depth to be 0.080% ± 0.029%. This result is in excellent agreement with the depth measured by Burton et al. (2012) of 0.088% ± 0.019%, and also consistent with the tentative detection of a significant eclipse in the optical ASTEP band by Abe et al. (2013), as well as deep NIR detections by Anderson et al. (2010) and Gibson et al. (2010). It is also in 2σ agreement with the measurement made using multiple eclipses from the 1.2 m Euler-Swiss telescope and the 0.6 m TRAPPIST telescope of 0.035% ± 0.012% (Lendl et al. 2013).

From the non-exhaustive set of VSTAR spectra, we find no single model that can fit all of the reported observations. However, when the spectrophotometry measurements by Bean et al.

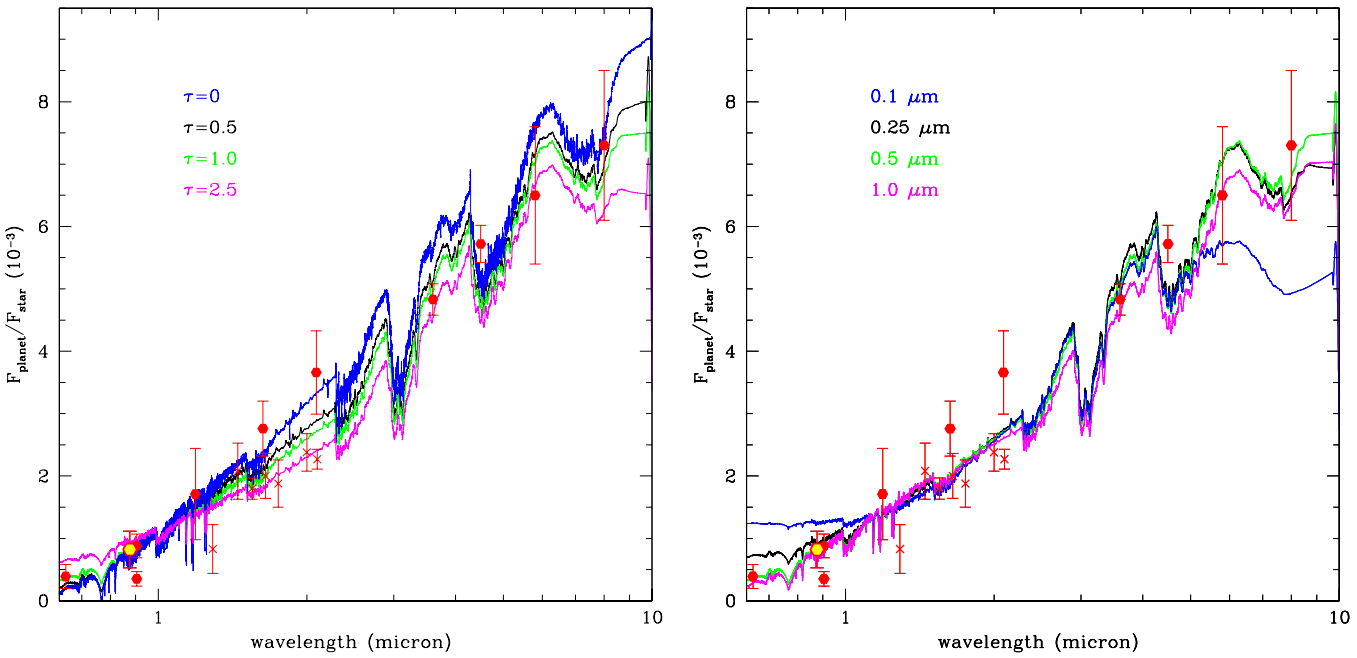

Figure 8. Model of the WASP-19b atmosphere with the *P–T* profile from Madhusudhan (2012) shown in Figure 6 and C/O = 1.1. Left: including clouds of varied opacity (τ) at the top of atmospheric layer, with a power-law distribution of particles with effective radius of 0.5 μm and effective variance 0.2 μm as defined in Mishchenko et al. (2002). Right: varying the mean particle size, while assuming $\tau = 1$ at 1.5 μm.

(A color version of this figure is available in the online journal.)

(2013) are discarded, the C/O enriched models present a good fit to the remaining points. The Bean et al. (2013) points are also inconsistent with available photometric J, H, K measurements at the same wavelengths. We also note that our new z-band detection is consistent in brightness temperature with the photometric NIR detections, but not the spectrophotometry measurement. These difficulties highlight the challenges of transit spectrophotometry observations, especially when WASP-19 is the faintest object targeted with the technique to date.

Line et al. (2013) assessed the difficulty of interpreting broadband emission spectra via retrieval techniques, and noted that C/O classifications tend toward a bimodal posterior of 0.5 or 1. This agrees with our assessment that large-scale changes in the spectrum are only apparent from C/O of 0.9 to 1.1. Although a quantitative estimate of carbon enrichment in these atmospheres is unlikely, WASP-19b is still more consistent with a super-solar C/O composition.

In addition to WASP-19b, Madhusudhan (2012) pointed to XO-1b, CoRoT-2b, WASP-33b, and WASP-12b as carbon-rich candidates. XO-1b is a significantly less irradiated planet that has only been studied in the *Spitzer* bands (Machalek et al. 2008). WASP-33 is a rapidly rotating F-dwarf that exhibits photometric variability on the hour timescale, for which precision photometry results are difficult to interpret (Smith et al. 2011). Light from WASP-12 was found to be contaminated by a blended M-dwarf, and the compensated eclipse measurements can be modeled without a carbon-rich atmosphere (Crossfield et al. 2012). Only CoRoT-2b has received as thorough an observational evaluation as WASP-19b, with measurements available from the *CoRoT* optical band to the *Spitzer* bands. No existing analysis has included all of the available observations to examine the validity of its carbon enriched claim.

This paper uses observations obtained with facilities of the Las Cumbres Observatory Global Telescope. The work was supported in part by the Australian Research Council through Discovery grant DP110103167. We acknowledge the recent *i*-band eclipse detection by Mancini et al. (2013), which could not be included within the time frame for the submission of this paper.

Facilities: FTS (Merope)

REFERENCES

Abe, L., Gonçalves, I., Agabi, A., et al. 2013, A&A, 553, A49
Anderson, D. R., Gillon, M., Maxted, P. F. L., et al. 2010, A&A, 513, L3
Anderson, D. R., Smith, A. M. S., Madhusudhan, N., et al. 2013, MNRAS, 430, 3422
Bailey, J., & Kedziora-Chudczer, L. 2012, MNRAS, 419, 1913
Barber, R. J., Tennyson, J., Harris, G. J., & Tolchenov, R. N. 2006, MNRAS, 368, 1087
Barman, T. S. 2008, ApJL, 676, L61
Bean, J. L., Désert, J.-M., Seifahrt, A., et al. 2013, ApJ, 771, 108
Bertin, E., & Arnouts, S. 1996, A&AS, 117, 393
Borysow, A., & Borysow, J. I. 1998, STIN, 99, 63017
Burrows, A., Hubeny, I., Budaj, J., Knutson, H. A., & Charbonneau, D. 2007, ApJL, 668, L171
Burrows, A., Ram, R. S., Bernath, P., Sharp, C. M., & Milsom, J. A. 2002, ApJ, 577, 986
Burrows, A., & Sharp, C. M. 1999, ApJ, 512, 843
Burton, J. R., Watson, C. A., Littlefair, S. P., et al. 2012, ApJS, 201, 36
Castelli, F., & Kurucz, R. L. 2004, arXiv:astro-ph/0405087
Chamberlain, S., Bailey, J., Crisp, D., & Meadows, V. 2013, Icar, 222, 364
Charbonneau, D., Allen, L. E., Megeath, S. T., et al. 2005, ApJ, 626, 523
Charbonneau, D., Brown, T. M., Noyes, R. W., & Gilliland, R. L. 2002, ApJ, 568, 377
Charbonneau, D., Knutson, H. A., Barman, T., et al. 2008, ApJ, 686, 1341
Cotton, D. V., Bailey, J., Crisp, D., & Meadows, V. S. 2012, Icar, 217, 570
Crossfield, I. J. M., Barman, T., Hansen, B. M. S., Tanaka, I., & Kodama, T. 2012, ApJ, 760, 140
Dulick, M., Bauschlicher, C. W., Jr., Burrows, A., et al. 2003, ApJ, 594, 651
Foreman-Mackey, D., Hogg, D. W., Lang, D., & Goodman, J. 2013, PASP, 125, 306
Fortney, J. J., Lodders, K., Marley, M. S., & Freedman, R. S. 2008, ApJ, 678, 1419
Fortney, J. J., Sudarsky, D., Hubeny, I., et al. 2003, ApJ, 589, 615

Fressin, F., Knutson, H. A., Charbonneau, D., et al. 2010, ApJ, 711, 374
Gibson, N. P., Aigrain, S., Pollacco, D. L., et al. 2010, MNRAS, 404, L114
Goorvitch, D. 1994, ApJS, 95, 535
Grillmair, C. J., Burrows, A., Charbonneau, D., et al. 2008, Natur, 456, 767
Gustafsson, B., Edvardsson, B., Eriksson, K., et al. 2008, A&A, 486, 951
Hargreaves, R. J., Hinkle, K. H., Bauschlicher, C. W., Jr., et al. 2010, AJ, 140, 919
Harris, G. J., Tennyson, J., Kaminsky, B. M., Pavlenko, Y. V., & Jones, H. R. A. 2006, MNRAS, 367, 400
Hebb, L., Collier-Cameron, A., Triaud, A. H. M. J., et al. 2010, ApJ, 708, 224
Hellier, C., Anderson, D. R., Collier-Cameron, A., et al. 2011, ApJL, 730, L31
Hubeny, I., Burrows, A., & Sudarsky, D. 2003, ApJ, 594, 1011
Kedziora-Chudczer, L., & Bailey, J. 2011, MNRAS, 414, 1483
Knutson, H. A., Howard, A. W., & Isaacson, H. 2010, ApJ, 720, 1569
Kovács, G., Bakos, G., & Noyes, R. W. 2005, MNRAS, 356, 557
Kupka, F., Piskunov, N., Ryabchikova, T. A., Stempels, H. C., & Weiss, W. W. 1999, A&AS, 138, 119
Lendl, M., Gillon, M., Queloz, D., et al. 2013, A&A, 552, A2
Line, M. R., Wolf, A., Zhang, X., et al. 2013, arXiv:1304.5561
Lodders, K. 2004, ApJ, 611, 587
López-Morales, M., Coughlin, J. L., Sing, D. K., et al. 2010, ApJL, 716, L36
Machalek, P., McCullough, P. R., Burke, C. J., et al. 2008, ApJ, 684, 1427
Madhusudhan, N. 2012, ApJ, 758, 36
Madhusudhan, N., & Seager, S. 2009, ApJ, 707, 24
Mancini, L., Ciceri, S., Chen, G., et al. 2013, arXiv:1306.6384
Mandel, K., & Agol, E. 2002, ApJL, 580, L171
Mishchenko, M. I., Travis, L. D., & Lacis, A. A. (ed.) 2002, Scattering, Absorption, and Emission of Light by Small Particles (Cambridge: Cambridge Univ. Press)
Öberg, K. I., Murray-Clay, R., & Bergin, E. A. 2011, ApJL, 743, L16
Piskunov, N. E., Kupka, F., Ryabchikova, T. A., Weiss, W. W., & Jeffery, C. S. 1995, A&AS, 112, 525
Plez, B. 1998, A&A, 337, 495
Pollack, J. B., Dalton, J. B., Grinspoon, D., et al. 1993, Icar, 103, 1
Pont, F., Knutson, H., Gilliland, R. L., Moutou, C., & Charbonneau, D. 2008, MNRAS, 385, 109
Rothman, L. S., Gordon, I. E., Barbe, A., et al. 2009, JQSRT, 110, 533
Showman, A. P., Fortney, J. J., Lian, Y., et al. 2009, ApJ, 699, 564
Skory, S., Weck, P. F., Stancil, P. C., & Kirby, K. 2003, ApJS, 148, 599
Smith, A. M. S., Anderson, D. R., Skillen, I., Collier Cameron, A., & Smalley, B. 2011, MNRAS, 416, 2096
Spiegel, D. S., Silverio, K., & Burrows, A. 2009, ApJ, 699, 1487
Swain, M. R., Vasisht, G., Tinetti, G., et al. 2009, ApJL, 690, L114
Tonry, J. L., Stubbs, C. W., Lykke, K. R., et al. 2012, ApJ, 750, 99
Weck, P. F., Schweitzer, A., Stancil, P. C., Hauschildt, P. H., & Kirby, K. 2003a, ApJ, 582, 1059
Weck, P. F., Stancil, P. C., & Kirby, K. 2003b, ApJ, 582, 1263
Winn, J. N., Holman, M. J., Torres, G., et al. 2008, ApJ, 683, 1076
Zahnle, K., Marley, M. S., Freedman, R. S., Lodders, K., & Fortney, J. J. 2009, ApJL, 701, L20
Zhou, G., & Bayliss, D. D. R. 2012, MNRAS, 426, 2483